Supporting Information

Inhibiting Jahn-Teller distortion of δ-MnO_2 cathode using 3d and 4d block elements doping to improve aqueous zinc ion battery performance

Priya Yadav,[a] Pragati,[a] Amit Kumar,[b] S.A. Hashmi,[b] Satendra Pal Singh,[c] Palash J. Thakuria,[d] Ankur K. Guha,[d] Arun Kumar Rai,[e] Alok Kumar Rai[a*]

[a]*Department of Chemistry, University of Delhi, Delhi 110007, India*

[b]*Department of Physics and Astrophysics, University of Delhi, Delhi 110007, India*

[c]*Department of Physics, University of Lucknow, Lucknow 226007, India*

[d]*Advanced Computational Chemistry Centre, Department of Chemistry, Cotton University, Panbazar, Guwahati, Assam 781001, India*

[e]*Raja Ramanna Centre for Advanced Technology, Indore, Madhya Pradesh 452013, India*

E-mail address:
***Corresponding author:** alokkumarrai1@gmail.com (A.K. Rai)

Table S1: Lattice parameters and Volume obtained after the Rietveld refinement.

S. No	Cathode Materials	a	b	c	β	Volume	Fraction of $Mn_{0.98}O_2$
1	Pure MnO_2	5.113(4)	2.8324(8)	7.356(3)	104.21(7)	103.3(1)	0
2	Fe doped-MnO_2	5.744(1)	2.781 (7)	7.375 (9)	104.77(2)	113.9(4)	54.23
3	Mo doped-MnO_2	6.226(3)	2.936(2)	7.273(4)	103.30(3)	129.4(1)	77.95
4	Rh doped-MnO_2	6.259(1)	2.877(4)	7.324(2)	104.4(1)	127.7(5)	26.42

1. Energy dispersive spectroscopy (EDS)

The selected regions used for EDS acquisition are shown in Figure S1 (a), (c), (e), and (g), while the corresponding EDX spectra are presented in Figures (b), (d), (f), and (h). For the pure δ-MnO_2 sample (Figures S1 b), the EDS spectrum displays strong Mn and O peaks, consistent with the expected MnO_2 composition. Minor signals from C and K are attributed to the substrate and residual precursors. In the Fe-doped δ-MnO_2 sample (Figures S1 d), the additional Fe peaks appear alongside Mn and O, confirming the incorporation of Fe into the MnO_2 matrix. For the Mo-doped δ-MnO_2 sample (Figures S1 f), the clear Mo peaks are observed in conjunction with Mn and O. The absence of any extraneous elements confirms the effective incorporation of Mo^{6+} into the MnO_2 lattice. Similarly, the Rh-doped δ-MnO_2 sample (Figures S1 h) exhibits distinct Rh peaks including Mn and O, indicating uniform and effective Rh incorporation. Overall, the EDS spectra of all the doped samples clearly verify the presence of Fe, Mo, and Rh, validating successful homogeneous elemental incorporation into the δ-MnO_2 framework. The absence of any impurity peaks further supports the phase purity and compositional integrity of the synthesized materials.

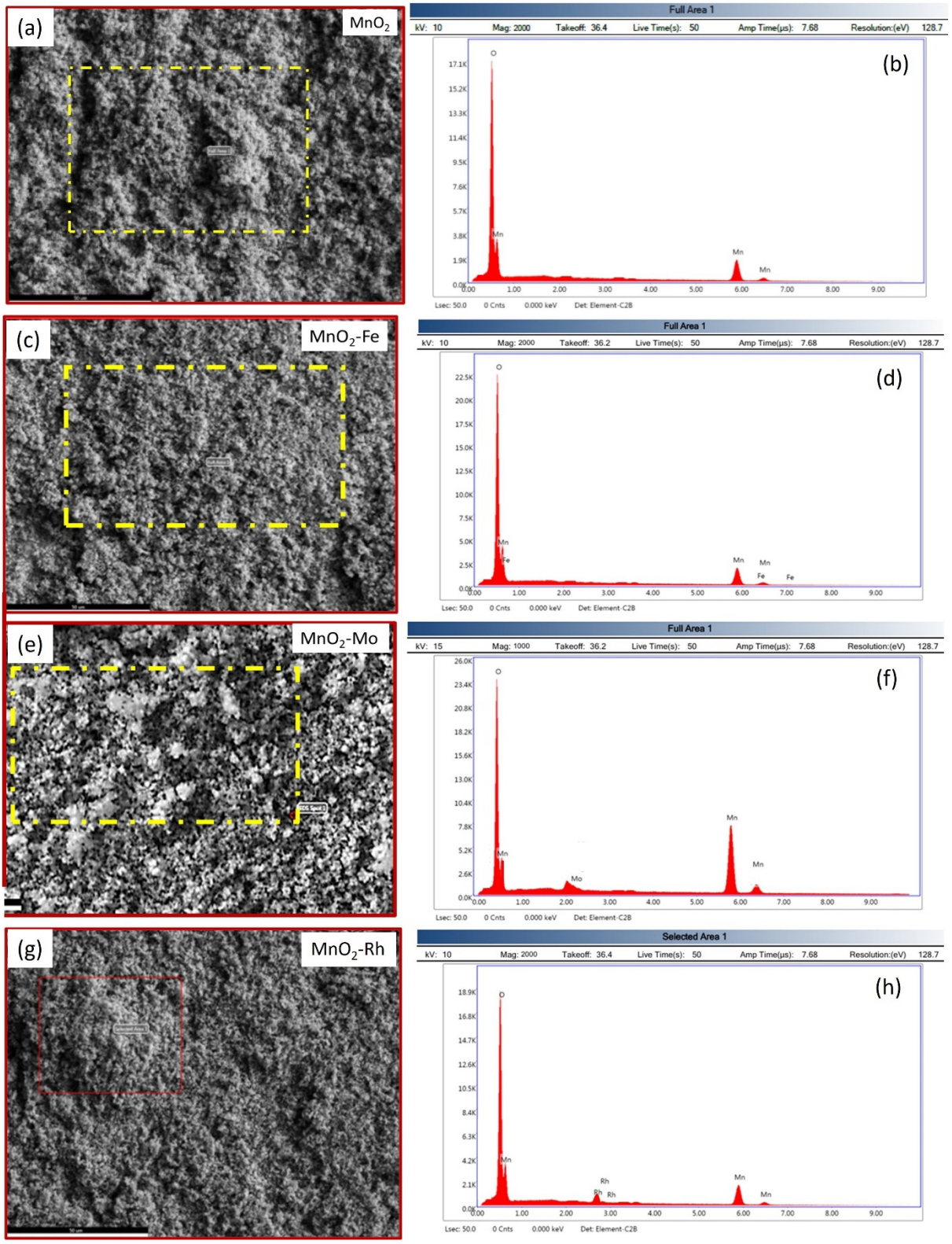

Figure S1: Energy dispersive spectroscopy (EDS) of (a-b) Pure; (c-d) Fe- doped; (e-f) Mo- doped and; (g-h) Rh- doped δ-MnO_2 samples, respectively.

2. Inductively coupled plasma mass spectrometry (ICP-MS) analysis:

As can be seen from the Table S2 that the dopant concentration is 75 ppb for Fe-doped δ-MnO_2 sample, which corresponds to an atomic percentage of 4.89 % relative to Mn. Likewise, the Mo-doped δ-MnO_2 sample shows a Mo concentration of 203.2 ppb, corresponding to an atomic percentage of 4.51%, whereas the Rh-doped δ-MnO_2 sample contains 241 ppb of Rh, giving an atomic percentage of 4.89%. The consistent atomic percentages across the three compositions indicate a comparable level of dopant incorporation in the δ-MnO_2 framework.

Table S2: Inductively coupled plasma mass spectrometry (ICP-MS) analysis of Fe- doped, Mo-doped and Rh- doped δ-MnO_2 cathode materials.

Cathode Materials	Concentration of Dopants (ppb)	Concentration of Mn (ppb)	Atomic %
Fe doped δ-MnO_2	75	1530.7	4.89
Mo doped δ-MnO_2	203.2	4503.6	4.51
Rh doped δ-MnO_2	241	4919.7	4.89

3. X-ray Fluorescence Spectroscopy (XRF) analysis:

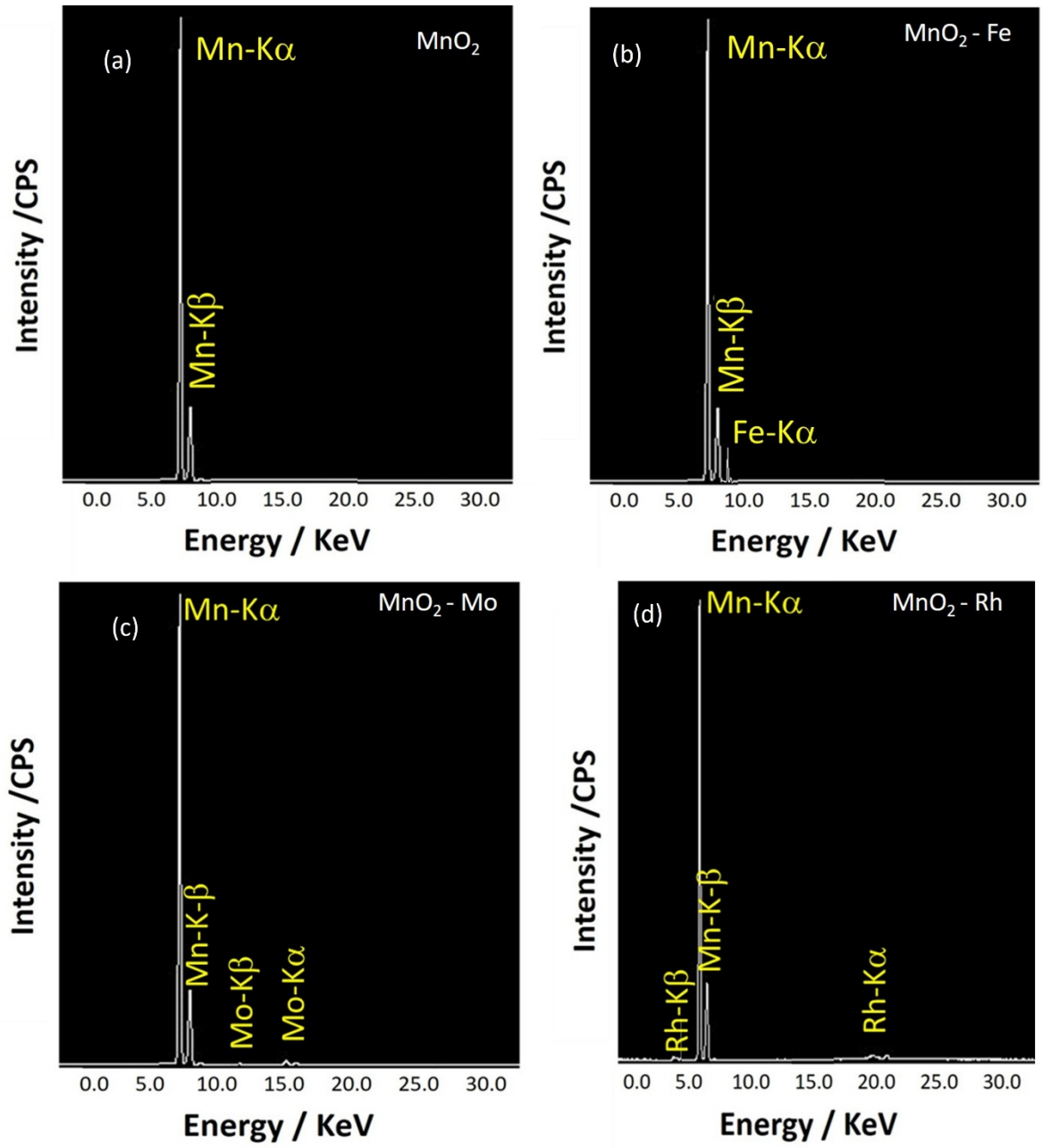

Figure S2: X-ray Fluorescence Spectroscopy (XRF) of (a) Pure; (b) Fe- doped; (c) Mo- doped and; (d) Rh- doped δ-MnO_2 samples.

4. BET analysis:

Based on the obtained isotherm data, the Fe^{3+}-doped δ-MnO_2 sample exhibits a high BET specific surface area of approximately 62 m^2 g^{-1}. In comparison, the Mo^{6+} -doped δ-MnO_2 sample shows a surface area of about 52.57 m^2 g^{-1}, followed by the Rh^{3+}-doped and pure δ-MnO_2 samples, with surface areas of approximately 43 m^2 g^{-1} and 30 m^2 g^{-1}, respectively. In

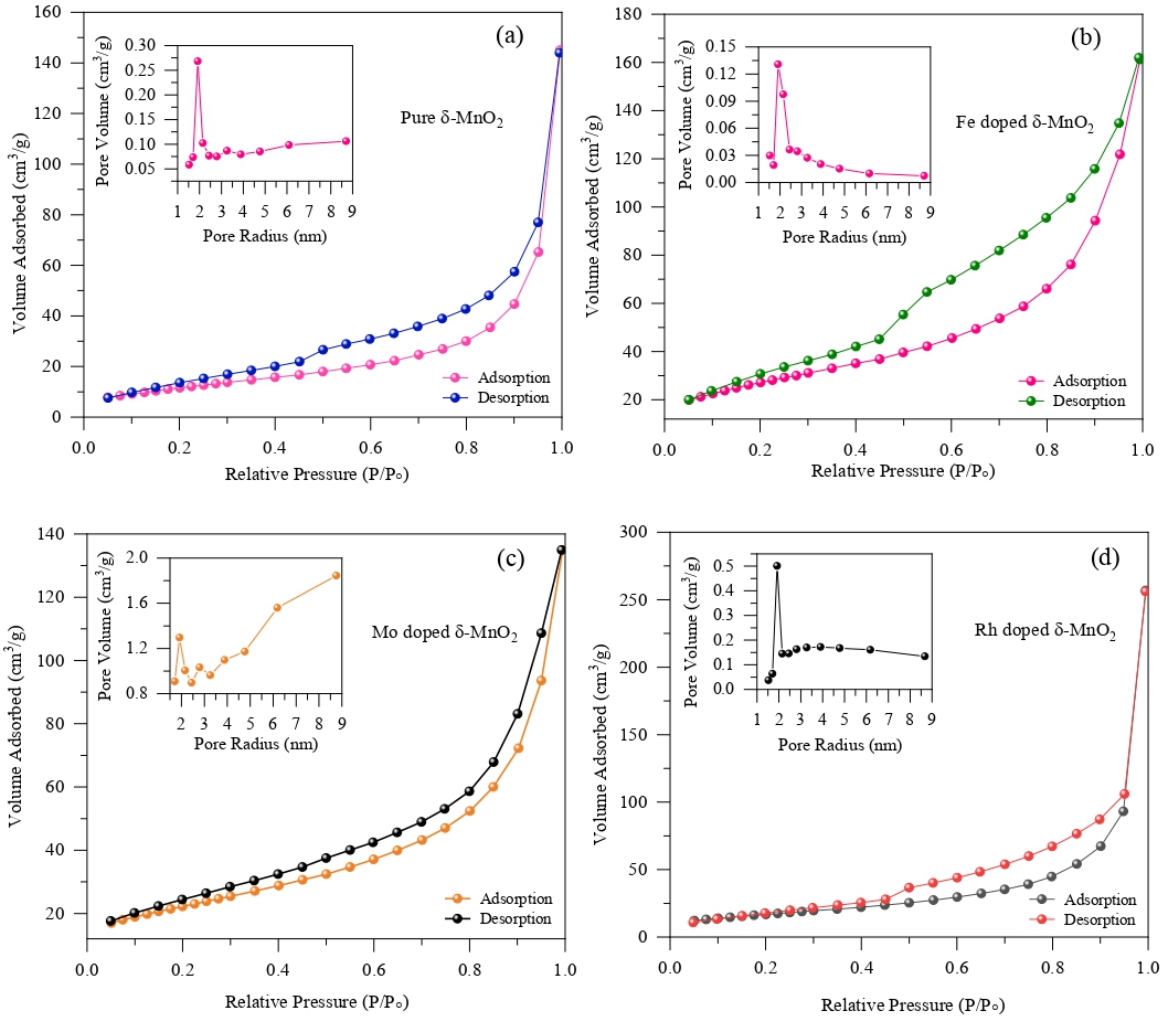

Figure S3: N_2 adsorption/desorption isotherm and BJH pore size distribution (inset) curves of the (a) pure δ-MnO_2; (b) Fe-doped δ-MnO_2; (c) Mo-doped δ-MnO_2 and; (d) Rh-doped δ-MnO_2 samples, respectively.

addition, the insets of Figure 5 (a-d) show the Barrett- Joyner–Halenda (BJH) pore size distribution curves, which demonstrates an average pore volume of ~0.061 $cm^3\ g^{-1}$ for pure, 0.125 $cm^3\ g^{-1}$ for Fe^{3+} doped, ~0.105 $cm^3\ g^{-1}$ for Mo^{6+} doped and 0.092 $cm^3\ g^{-1}$ for Rh^{3+} doped δ-MnO_2 samples. Since a large surface area inherently offers more electroactive sites, thereby enhanced Faradaic reactions, a uniform and well distributed pores can also significantly augment energy conversion efficiency by shortening the diffusion pathways of charge carriers. [23] The Rh^{3+} doped sample initially shows better result than pure δ-MnO_2 but Fe^{3+} and Mo^{6+} doping appears to be much more promising and comparatively exhibits excellent porous properties than pure and Rh^{3+} doped sample. The large surface area with mesoporous structure

of Fe^{3+} and Mo^{6+} doped samples may facilitate sufficient electrolyte into internal pores followed by offering of plenty of electrochemical active sites and enough spaces to tackle the mechanical stresses occurred during numerous Zn^{2+} ions discharge/charge processes.

5. Computational Details:

For the sake of computation, we have considered a unit cells of δ-MnO_2 and Fe doped δ-MnO_2 and optimized the geometry using PBE0/def2-TZVP level. [47] Harmonic vibrational frequency calculations confirm that the optimized geometries are at their local minima with all real values of the Hessian matrix. All these calculations were performed using GAUSSIAN16 suite of program.[48] Projected density of states (PDOS) calculations was performed using Multiwfn program code.[49]

5.1 Results and Discussion:

Figure S4 shows the optimized geometries of undoped δ-MnO_2 and Fe doped δ-MnO_2. In the undoped δ-MnO_2, the axial Mn-O bonds are longer (1.93 Å) than the equatorial Mn-O bond distances (1.87 Å). This is a clear indication of Jahn-Teller (JT) distortion. Due to the unsymmetrical occupancies of e_g set of d orbital (d_Z^2 and $d_{X^2-Y^2}$) in Mn^{3+} state, elongation along Z-axis arises which lowers the symmetry and removes the degeneracy (Figure S5). At 5% Fe^{3+} doping, JT distortion almost vanishes making the axis Mn-O and equatorial Mn-O bond lengths almost equal (1.88 Å axial and 1.87 Å equatorial). Thus, from the geometrical point of view, it is clear that Fe^{3+} doping to δ-MnO_2 reduces JT distortion.

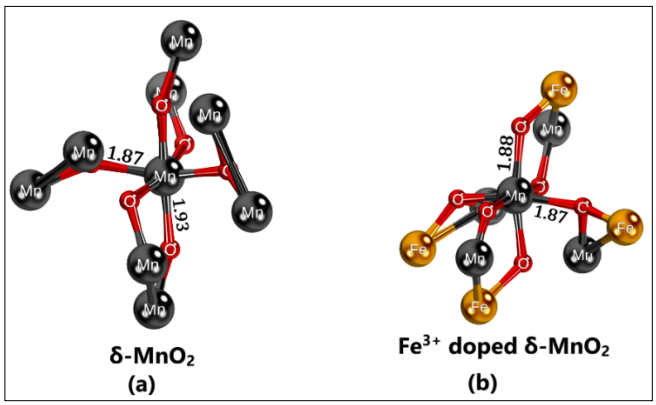

Figure S4. Optimized geometries of (a) undoped δ-MnO_2 and (b) Fe^{3+} doped δ-MnO_2. Bond lengths are in Å.

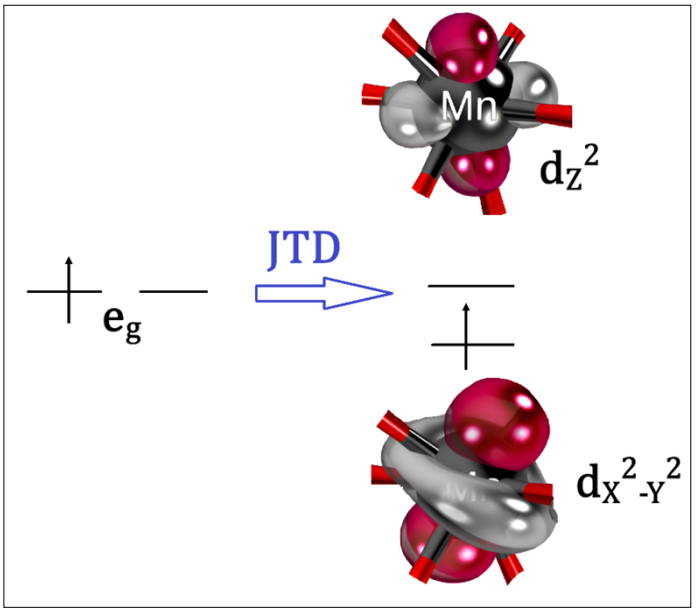

Figure S5. Splitting of e_g set due to JT distortion in δ-MnO_2 with the lower energy $d_{X^2-Y^2}$ being singly occupied in the distorted δ-MnO_2 complex.

We also tried to optimize the geometries of the Rh and Mo doped δ-MnO_2 structures, however, the unit cell completely lost symmetry and resulted in unoptimized structure. This might be due to the mismatch in the size of Rh and Mo compared to that Mn, thereby replacing Mn^{3+} ions by Rh^{3+} and Mo^{3+} in δ-MnO_2 may destroy the structural unity. Therefore, the theoretical results will be discussed on the undoped δ-MnO_2 and Fe^{3+} doped δ-MnO_2 only.

To understand why Fe^{3+} doping relaxes JT distortion, we plotted the density of states of both δ-MnO_2 and Fe^{3+} doped δ-MnO_2 (Figure S6). It is evident that d-band of Fe overlaps with the d-band of Mn, thereby indicating a possibility that Fe^{3+} will either oxidize Mn^{3+} to JT distortion relaxed Mn^{4+} state or reduce Mn^{3+} to Mn^{2+}. It should be noted that both Mn^{4+} and Mn^{2+} do not show JT distortion. Calculation of the natural charge at the central Mn atom indicates that there is reduction of positive charge from 0.78 e to 0.23 e in going from δ-MnO_2 to Fe^{3+} doped δ-MnO_2. This indicates that Fe^{3+} has reduced Mn^{3+} to Mn^{2+} and this one electron reduction process mediated by Fe^{3+} relaxes the JT distortion.

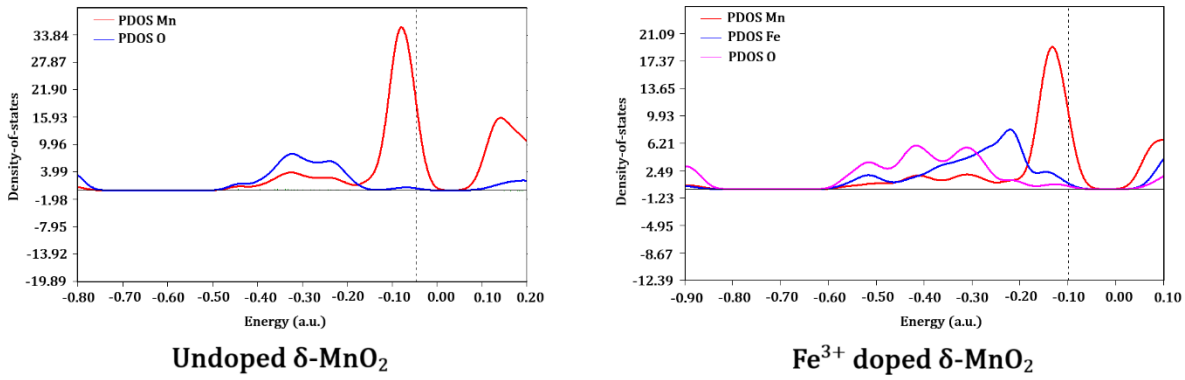

Figure S6. Projected density of states (PDOS) for undoped δ-MnO_2 and Fe^{3+} doped δ-MnO_2.

Table S3: A comparison between the specific capacities of our work and previously reported δ-MnO_2 electrodes.

S. No.	Material	Morphology	Specific Capacity /Cycle Number/ Current densities	Ref.
1.	δ-MnO_2	Nanosheets	126 mAh g^{-1} after 100 cycles at 100 mAg^{-1}	8
2.	Ca doped δ-MnO_2	Nanoflower	124 mAh g^{-1} at 1000 cycles at 1.5 Ag^{-1}	24
3.	N and S doped δ-MnO_2	Nanoflower	120 mAh g^{-1} at 1500 cycles at 1 Ag^{-1}	25
4.	δ-MnO_2	Flower-like	70 mAh g^{-1} after 100 cycles at 100 mAg^{-1}	42
5.	Ni doped δ-MnO_2	Nanoparticles	72 mAh g^{-1} after 600 cycles at 1 Ag^{-1}	43
6.	δ-MnO_2/ graphite	Nanoflower	114 mAh g^{-1} after 100 cycles at 400 mAg^{-1}	44
7.	δ-MnO_2/CNT	Flower-like	96 mAh g^{-1} after 100 cycles at 400 mAg^{-1}	45
8.	Fe doped δ-MnO_2	Flower-like microspheres	48.74 mAh g^{-1} at 200 cycles at 0.5 Ag^{-1}	46
9.	Fe doped δ-MnO_2 Mo doped δ-MnO_2 Rh doped δ-MnO_2	Nanoflower Hawthorn like Nanoflower	100.51 mAh g^{-1} at 530 cycles at 2 C 155.2 mAh g^{-1} at 530 cycles at 2 C 83.03 mAh g^{-1} at 530 cycles at 2 C	Our work